Beyond Fullerenes: Design of Nonfullerene Acceptors for Efficient Organic Photovoltaics

Haiyan Li,[†] Taeshik Earmme,[†] Guoqiang Ren,[†] Akinori Saeki,[‡,§] Saya Yoshikawa,[‡] Nishit M. Murari,[†] Selvam Subramaniyan,[†] Matthew J. Crane,[†] Shu Seki,[‡] and Samson A. Jenekhe*,[†]

[†]Department of Chemical Engineering and Department of Chemistry, University of Washington, 36 Bagley Hall, Seattle, Washington 98195-1750, United States

[‡]Department of Applied Chemistry, Graduate School of Engineering, Osaka University, 2-1 Yamadaoka, Suita, Osaka 565-0871, Japan

[§]PRESTO, Japan Science and Technology Agency (JST), 4-1-8 Honcho Kawaguchi, Saitama, Saitama 332-0012, Japan

S Supporting Information

ABSTRACT: New electron-acceptor materials are long sought to overcome the small photovoltage, high-cost, poor photochemical stability, and other limitations of fullerene-based organic photovoltaics. However, all known nonfullerene acceptors have so far shown inferior photovoltaic properties compared to fullerene benchmark [6,6]-phenyl-C_{60}-butyric acid methyl ester ($PC_{60}BM$), and there are as yet no established design principles for realizing improved materials.

Herein we report a design strategy that has produced a novel multichromophoric, large size, nonplanar three-dimensional (3D) organic molecule, DBFI-T, whose π-conjugated framework occupies space comparable to an aggregate of 9 [C_{60}]-fullerene molecules. Comparative studies of DBFI-T with its planar monomeric analogue (BFI-P2) and $PC_{60}BM$ in bulk heterojunction (BHJ) solar cells, by using a common thiazolothiazole-dithienosilole copolymer donor (PSEHTT), showed that DBFI-T has superior charge photogeneration and photovoltaic properties; PSEHTT:DBFI-T solar cells combined a high short-circuit current (10.14 mA/cm^2) with a high open-circuit voltage (0.86 V) to give a power conversion efficiency of 5.0%. The external quantum efficiency spectrum of PSEHTT:DBFI-T devices had peaks of 60−65% in the 380−620 nm range, demonstrating that both hole transfer from photoexcited DBFI-T to PSEHTT and electron transfer from photoexcited PSEHTT to DBFI-T contribute substantially to charge photogeneration. The superior charge photogeneration and electron-accepting properties of DBFI-T were further confirmed by independent Xenon-flash time-resolved microwave conductivity measurements, which correctly predict the relative magnitudes of the conversion efficiencies of the BHJ solar cells: PSEHTT:DBFI-T > PSEHTT:$PC_{60}BM$ > PSEHTT:BFI-P2. The results demonstrate that the large size, multichromophoric, nonplanar 3D molecular design is a promising approach to more efficient organic photovoltaic materials.
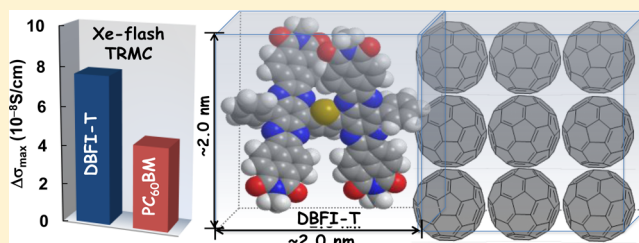
INTRODUCTION

Fullerene-based electron acceptors have provided the foundation for advances in fundamental understanding of charge photogeneration and practical developments in organic photovoltaics (OPVs) in the last 20 years.[1−6] The power conversion efficiency (PCE) of single-junction OPV cells has steadily increased from 2.5% to current 7−9% as the donor polymer paired with a fullerene derivative has changed from poly-(phenylenevinylene) derivatives[7] to poly(3-hexylthiophene)[8] to numerous narrow band gap copolymers.[9−11] Fullerene derivatives, such as [6,6]-phenyl-C_{60}-butyric acid methyl ester ($PC_{60}BM$) (Figure S1), have remained the most investigated electron-acceptor materials in OPVs because of their overall outstanding charge photogeneration and transport properties.[6−11] The prospects of enabling new pathways to OPVs while overcoming the small photovoltage, high cost, photochemical stability, and other limitations of fullerene-based OPVs have motivated efforts to discover alternative electron-acceptor materials.[12−27] However, all nonfullerene acceptors reported so far have shown substantially inferior electron-accepting and photovoltaic properties in bulk heterojunction (BHJ) solar cells. Vacuum-deposited small molecule planar heterojunction cells with C_{60}-doped electron transport layer have recently been reported to show PCEs of up to 6.4%.[28−30] Solution processed OPVs including polymer-donor/small-molecule-acceptor OPVs[12−27] and polymer-donor/polymer-acceptor (all-polymer) OPVs[31−36] showed lower performance with PCEs 3−4%. Recently, polymer/polymer blend (all-polymer) solar cells with PCEs of up to 4.8% have been reported,[37,38] whereas polymer-donor/small-molecule-acceptor solar cells using a fullerene self-assembled monolayer ($PC_{60}BM$-SAM) interface modifier have resulted in a 6% PCE.[39] Unlike the development of donor (p-type) conjugated polymers,[40−42] there are as yet no general guiding principles for

the design of electron-acceptor (n-type) materials for OPVs.[12−27]

Toward this end, recent studies have highlighted some special attributes that make fullerene derivatives such as $PC_{60}BM$ so successful as electron acceptors in OPVs:[43−52] (i) the existence of low-lying excited states in their monoanions, which leads to substantial enhancement in charge separation rates without affecting the charge recombination rate;[43−45] (ii) their large π-conjugated molecular structure which supports efficient electronic delocalization and polaron formation;[46,47] (iii) their rigid molecular architecture and high molecular diffusion that facilitate facile aggregation into a phase-separated nanoscale morphology for efficient charge separation and transport;[8,11,48,52] and (iv) their three-dimensional (3D) spherical structure, which results in a large decrease in Coulomb barrier for charge separation due to enhanced entropic effects[49] and enables isotropic charge transport.[50,51] To date, however, these recent insights are yet to be exploited to design and experimentally realize new nonfullerene-acceptor materials that facilitate efficient charge photogeneration, isotropic charge transport, and photovoltaic properties comparable to the PCBMs.

Herein we propose and test a strategy for the molecular design of nonfullerene electron-acceptor materials for highly efficient OPVs by translating some of the above theoretical insights from studies of fullerene-PCBMs into a concrete experimental molecular engineering of materials. The approach includes the following four main design criteria. (1) The molecule should have an overall large, rigid, π-conjugated electron-deficient framework that is comparable or larger than C_{60}: this is to ensure facile exciton and charge delocalization and nanometer-sized molecular objects that can mix with a donor semiconducting polymer or molecule while facilitating good electron transport.[52] (2) The molecule should have a large density of states at the lowest unoccupied molecular orbital (LUMO) and existence of low-lying excited states of the monoanions: this is to ensure a large charge separation rate.[43] (3) The molecule should have a nonplanar 3D architecture: this criterion aims to avoid the efficient formation of intermolecular exciplexes at donor/acceptor interfaces[3,45,53] while facilitating good isotropic electron transport[50,51] even in a poorly crystalline thin film; enhanced charge separation due to entropic effects may also result.[49] (4) The molecule should have a multichromophoric architecture such as a dimer or higher oligomer: this provides a means to enhance the density of states at the LUMO,[43] achieve nonplanar 3D conformation, and enlarge the π-conjugated framework. We have used these criteria to design and synthesize two related new π-conjugated acceptor molecules for comparison with the $PC_{60}BM$ benchmark: 8,17-diphenyl-7,9,16,18-tetraazabenzodifluoranthene-3,4,12,13-tetracarboxylic acid diimide (BFI-P2, Figure 1a) and 2,5-bis(8-(17-phenyl)-7,9,16,18-tetraazabenzodifluoranthene-3,4,12,13-tetracarboxylic acid diimide)thiophene (DBFI-T, Figure 1b,c). We used DFT calculations to examine the molecular geometries and electronic structures of the new acceptor molecules. We have performed comparative studies of the charge photogeneration and photovoltaic properties of the new acceptors (BFI-P2, DBFI-T) and $PC_{60}BM$ by using a known donor polymer, PSEHTT, and fabricating and evaluating both conventional and inverted BHJ solar cells. Charge transport in neat films of BFI-P2 and DBFI-T was investigated by using organic field-effect transistors (OFETs), while bulk charge transport in BHJ active layers was studied by
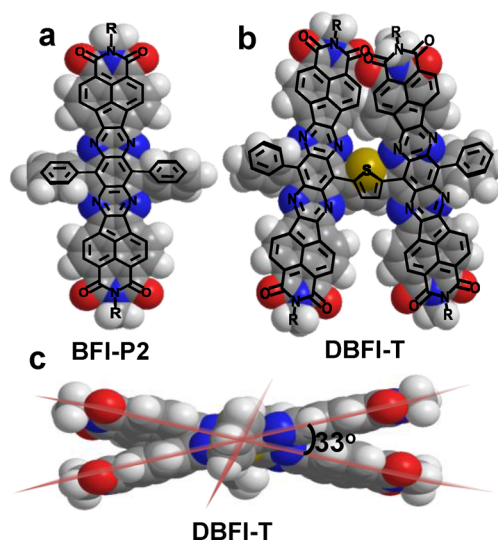

Figure 1. Molecular structures overlaid with the space filling structure of BFI-P2 (a) and DBFI-T (b) and side view of the space filling structure of DBFI-T after geometry optimization (c).

the space-charge-limited current (SCLC) method. Surface and bulk morphologies of polymer/acceptor blend active layers were studied by atomic force microscopy (AFM) and X-ray diffraction (XRD), respectively. Finally, transient photoconductivity and intrinsic charge photogeneration properties of the polymer/acceptor blend films were examined by time-resolved microwave conductivity studies.

■ RESULTS AND DISUSSION

Molecular Design and Theoretical Calculations. The geometry optimized molecular structures of BFI-P2 and DBFI-T using density functional theory (DFT) at the B3LYP/6-31G(d) level are shown in Figure 1a−c. The ladder-type BFI chromophore in BFI-P2 is perfectly planar, and the calculated end-to-end distance between the imide nitrogen atoms of BFI-P2 is 19.7 Å in excellent agreement with the same distance measured from the reported X-ray single crystal structure (19.6 Å) of the parent BFI molecule;[54] the distance between *para* carbon atoms of the two phenyl group is 11.5 Å (Figure S2 and Table S2). In the case of DBFI-T, the molecule has the same 19.7 Å long planar BFI units and an end-to-end width of 19.5 Å at the middle (distance between *para* carbon atoms of each phenyl) (Figure S2 and Table S3), which means 101 π-atoms ($C_{84}N_8O_8S$) densely pack into a nearly 2.0× 2.0 × 0.6 nm³ space. The two BFI units in DBFI-T are strongly twisted with interplanar angle of 32.7° due to steric hindrance, resulting in an overall nonplanar 3D structure (Figure 1c). Notably, the π-conjugated backbone of DBFI-T molecule is significantly larger than C_{60} (~7.1 Å in diameter for C_{60})[55] (Figure S3); the calculated Connolly solvent excluded volume of DBFI-T (1046.9 ų) is more than twice of that of C_{60} (477.7 ų). The interaction volume that a single DBFI-T molecule presents to a donor polymer is roughly equivalent to that of nine fullerene molecules (Figure S3). The significantly larger π-conjugated structure of DBFI-T could be expected to facilitate molecular orbital coupling, exciton, and charge delocalization over a single molecule or multiple molecules and benefit charge separation and electron transport properties.[46,47,52]

The frontier orbital energy levels of DBFI-T and BFI-P2 and the low-lying excited states of their monoanions were also

calculated at the same B3LYP/6-31G(d) level to evaluate the potential electron accepting ability of the new acceptors. We found that the neutral DBFI-T has 6 quasi-degenerate LUMOs with close energy levels (−3.35 to −3.04 eV) (Figures 2a and S4),
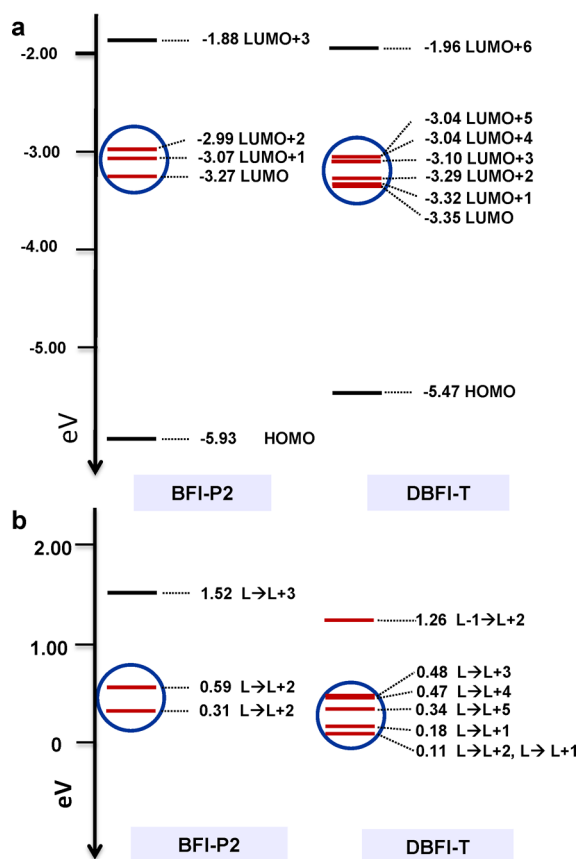

Figure 2. Calculated quasi degenerate LUMO energy levels of the optimized BFI-P2 and DBFI-T (a) and low-lying excited states of BFI-P2 and DBFI-T anions (b) using DFT calculations (B3LYP/6-31G(d)).

while its radical anion has 5 low-lying excited states (<0.5 eV) (Figure 2b). In contrast, the neutral BFI-P2 has three quasi-degenerate LUMOs (−3.27 to −2.99 eV) (Figures 2a and S5), whereas its radical anion has only two low-energy excited states (<0.6 eV) (Figure 2b). These initial simulation results are to be compared with the recent theoretical results for the benchmark $PC_{60}BM$, which has three quasi-degenerate LUMOs and its monanion has two low-energy excited states.[43] The large density of states at the LUMO of the multichromophoric DBFI-T and its monoanion suggest that DBFI-T is a potentially superior electron acceptor than BFI-P2 or $PC_{60}BM$ in OPVs.[43]

Synthesis, Absorption Spectra, Electronic Structure, and Charge Transport Properties. Both BFI-P2 and DBFI-T were synthesized from the previously reported electron-deficient 8,17-dibromo-7,9,16,18-tetraazabenzodifluoranthene-3,4,12,13-tetracarboxylic acid diimide (BFI-Br2) building block[54] (Scheme 1). The molecular structures of BFI-P2 and DBFI-T were confirmed by high-resolution mass spectroscopy, elemental analysis, and NMR spectroscopy. Both BFI-P2 and DBFI-T have excellent solubility in organic solvents (chloroform, toluene, chlorobenzene, etc.) and are thus suitable for spin coating, printing, and other solution processing methods.

Scheme 1. Synthesis of BFI-P2 and DBFI-T
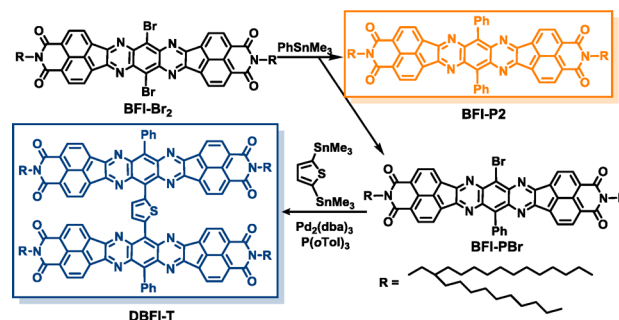
Thermogravimetric analysis of BFI-P2 and DBFI-T showed that both molecules were thermally stable up to 430−440 °C (Figure S7), indicating robust thermal stability desirable for OPV applications. Differential scanning calorimetry (DSC) scans of BFI-P2 from 20 to 300 °C showed intense crystalline melting and recrystallization peaks at 259 and 208 °C, respectively (Figure S8). Similar DSC scans of DBFI-T showed only a broad shallow endotherm centered at 224 °C in the heating cycle with no transition in the cooling cycle, indicating a poorly crystalline material.

Optical absorption and electronic structure of spin coated thin films of BFI-P2 and DBFI-T were characterized by optical absorption spectroscopy and cyclic voltammetry (Figure 3 and
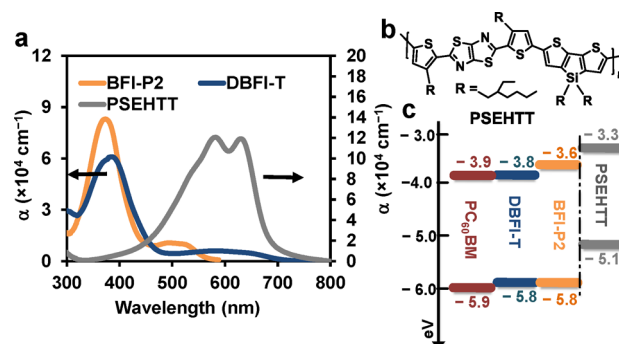

Figure 3. Thin-film optical absorption spectra of new acceptors (BFI-P2 and DBFI-T) and donor polymer PSEHTT (a), molecular structure of PSEHTT (b), and energy levels of donor polymer (PSEHTT), new nonfullerene acceptors (BFI-P2 and DBFI-T), and $PC_{60}BM$ (c).

Table S1). The thin-film absorption spectrum of BFI-P2 is comprised of an intense UV band centered at 374 nm with an absorption coefficient of 8.7×10^4 cm^{-1} and a weak, broad, visible band centered at ∼500 nm ($\alpha = 1.6 \times 10^4$ cm^{-1}). The former absorption band arises from the $\pi−\pi^*$ transition of the BFI chromophore,[54] while the latter band is due to delocalization into the phenyl rings. In contrast, the thin-film absorption spectrum of the multichromophoric DBFI-T has a slightly red-shifted intense UV band ($\lambda_{max} = 387$ nm, $\alpha = 6.5 \times 10^4$ cm^{-1}) and a very broad visible band centered near 600 nm ($\alpha = 6.1 \times 10^3$ cm^{-1}). The visible absorption band of DBFI-T is due to intramolecular charge transfer between the central thiophene ring and the BFI units. The absorption spectrum of the thiazolothiazole-dithienosilole copolymer PSEHTT (Figure 3b) shows a broad visible band with a maximum at 584 nm and a high absorption coefficient (1.1×10^5 cm^{-1}), indicating a promising donor component[56,57] that could be paired with the

new nonfullerene acceptors in BHJ solar cells. The frontier molecular orbital (HOMO/LUMO) energy levels of BFI-P2 and DBFI-T were estimated from cyclic voltammetry and are shown in the diagram of Figure 3c in comparison to our measured HOMO/LUMO energy levels for the donor polymer PSEHTT and $PC_{60}BM$. These data indicate that there is sufficient driving energy for photoinduced electron transfer in BHJ devices composed of PSEHTT and DBFI-T as well as with the fullerene acceptor. However, the LUMO offset of 0.3 eV between BFI-P2 and PSEHTT is comparably smaller, and this may result in difference in photoinduced electron transfer efficiency of PSEHTT:BFI-P2 blend compared to those of PSEHTT:DBFI-T and PSEHTT:$PC_{60}BM$ blends. PSEHTT:$PC_{60}BM$ blend BHJ solar cells have indeed previously been reported.[56] The slightly higher lying LUMO energies of BFI-P2 and DBFI-T suggest a likely improvement in the open circuit voltage (V_{oc}) of the nonfullerene-acceptor/PSEHTT devices compared to PSEHTT/fullerene ones.

Charge transport in neat, spin coated, BFI-P2 and DBFI-T thin films was investigated by using top-contact bottom-gate organic field-effect transistors (OFETs). The OFETs were fabricated on octyltrichlorosilane (OTS8)-modified SiO_2/Si substrates with silver source and drain electrodes. The output and transfer curves (Figure S11) showed that both BFI-P2 and DBFI-T OFETs exhibited unipolar n-channel transport characteristics. BFI-P2 had a maximum electron mobility (μ_e) of 0.5 cm^2/(V s) (0.2 cm^2/(V s), average) with an $I_{on/off}$ ratio of 10^6, while DBFI-T had a much lower electron mobility of 0.006 cm^2/(V s). The poor crystallinity of DBFI-T thin films can account for its much lower electron mobility than BFI-P2. Nevertheless, the observed electron mobilities in BFI-P2 and DBFI-T are higher or comparable to those seen in $PC_{60}BM$.[58]

Nonfullerene Organic Solar Cells. BHJ solar cells incorporating DBFI-T, BFI-P2, and $PC_{60}BM$, respectively, were fabricated and evaluated using a common test donor polymer, PSEHTT (Figure 3b). Conventional cells with a structure of indium tin oxide (ITO)/poly(3,4-ethylenedioxythiophene):poly(styrenesulfonate) (PE-DOT:PSS)/PSEHTT:DBFI-T/LiF/Al (Figure 4a) were fabricated and the current density–voltage (J–V) characteristics were evaluated under AM1.5 solar illumination at 1 sun (100 mW/cm^2). Optimization of the blend active layer composition showed that 1:2 (w/w) PSEHTT:DBFI-T photodiodes gave the best PCE of 4.24%, V_{oc} of 0.82 V, short circuit current (J_{sc}) of 9.02 mA/cm^2, and a fill factor (FF) of 57% (Figure 4b, Table 1). The external quantum efficiency (EQE) spectrum of the PSEHTT:DBFI-T photodiode (Figure 4c) shows that the photocurrent turns on at about 720 nm and has peaks of 53% at 380–420 nm and 51% at 540–620 nm due, respectively, to the DBFI-T and PSEHTT components. The J_{sc} calculated from the EQE spectrum is 8.30 mA/cm^2, which is 8.7% lower than from the direct J–V measurement. Similarly fabricated and tested PSEHTT:BFI-P2 blend (1:4 w/w) photodiodes gave the best performance with PCE = 1.03%, J_{sc} = 2.31 mA/cm^2, V_{oc} = 0.90 V, and FF = 49% (Figure S12). Although the V_{oc} of BFI-P2 solar cells is higher than that of DBFI-T, as expected from their LUMO energy levels (Figure 3c), the photocurrent and PCE of BFI-P2 devices are about a factor of 4 lower. These results show that DBFI-T has a far superior photovoltaic performance in OPV cells than BFI-P2.

Inverted solar cells with the structure ITO/zinc oxide (ZnO)/PSEHTT:DBFI-T/molybdenum oxide/(MoO_3)/Ag (Figure 4d) were also fabricated and evaluated to further
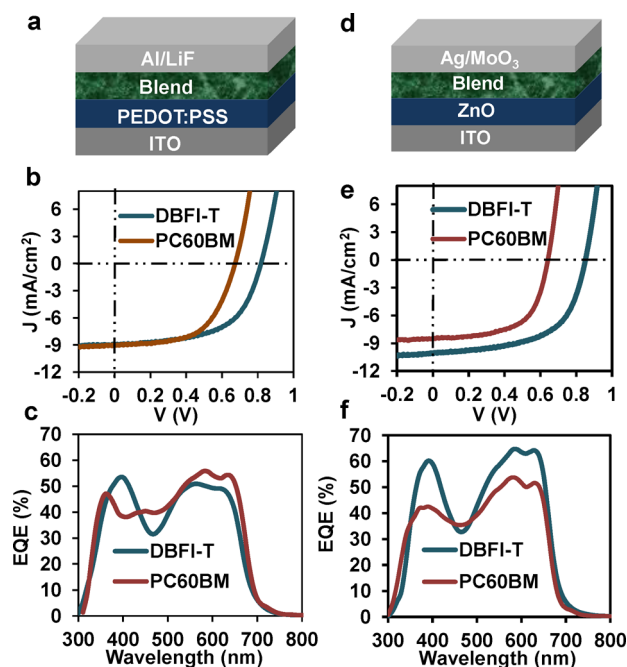
Figure 4. Comparison of J–V characteristics and EQE spectra of PSEHTT:DBFI-T BHJ solar cells with PSEHTT:$PC_{60}BM$ BHJ solar cells. Schematic of the conventional cell (a), and comparison of J–V curves (b) and EQE spectra (c) of the conventional solar cells based on the PSEHTT:DBFI-T (1:2 w/w) blend and based on the PSEHTT:$PC_{60}BM$ (1:2 w/w) blend. Schematic of inverted cell (d), and comparison of J–V curves (e) and EQE spectra (f) of inverted solar cells based on the PSEHTT:DBFI-T (1:2 w/w) blend and based on the PSEHTT:$PC_{60}BM$ (1:2 w/w) blend.

investigate the photovoltaic properties of the new electron acceptors. In this case, the optimum PSEHTT:DBFI-T (1:2 w/w) photodiodes with the surface of ZnO modified by a thin layer of ethanolamine gave a higher PCE of 5.04% with V_{oc} = 0.86 V, J_{sc} = 10.14 mA/cm^2, and FF = 58% (Figure 4e and Table 1). The corresponding EQE spectrum of the optimum photodiodes showed a peak value of 65% in the 550–620 nm range and 60% in the 380–420 nm range (Figure 4f). The J_{sc} value of 9.82 mA/cm^2 calculated from the EQE spectrum is within 3% of the value measured directly from the J–V curve. The optimum inverted PSEHTT:BFI-P2 blend (1:4 w/w) cells had a PCE of 1.44% with J_{sc} = 3.16 mA/cm^2, V_{oc} = 0.94 V, and FF = 49% (Figure S13). These results further confirm the excellent charge photogeneration and photovoltaic properties of DBFI-T.

The conventional and inverted BHJ solar cells of the benchmark PSEHTT:$PC_{60}BM$ (1:2 w/w) were fabricated by using previously reported optimized conditions.[56] The results (Table 1 and Figure 4) show that both conventional and inverted PSEHTT:$PC_{60}BM$ photodiodes with maximum PCEs of 3.34–3.55% are significantly better than the corresponding BFI-P2 devices, whereas they are substantially inferior to those of PSEHTT:DBFI-T devices with efficiencies of 4.24–5.04%. It is notable that DBFI-T devices have similar FFs and photocurrents as those of $PC_{60}BM$ devices but have significantly larger photovoltages (Figure 4 and Table 1). The much lower photocurrents and lower FFs of BFI-P2 devices compared to either $PC_{60}BM$ or DBFI-T may imply that charge photogeneration and charge collection are less efficient in BFI-P2 devices. Poor charge collection efficiency may arise from

Table 1. Photovoltaic Properties of PSEHTT:Acceptor BHJ Solar Cells

device	acceptor[a]	J_{sc} (mA/cm²)	V_{oc}(V)	FF (%)	PCE(%)	PCE_{max}(%)
	DBFI-T[b]	**9.02**	**0.82**	**57**	**4.19 ± 0.05**	**4.24**
conventional cell	BFI-P2[c]	2.31	0.90	49	0.99 ± 0.06	1.03
	$PC_{60}BM$[d]	9.07	0.68	58	3.49 ± 0.06	3.55
	DBFI-T[e]	**10.14**	**0.86**	**58**	**4.91 ± 0.13**	**5.04**
inverted cell	BFI-P2[f]	3.16	0.94	49	1.39 ± 0.05	1.44
	$PC_{60}BM$[d]	8.46	0.64	62	3.23 ± 0.11	3.34

[a]All active layers were deposited from chloroform solutions. [b]PSEHTT:DBFI-T at 1:2 (w/w), annealing at 175 °C for 10 min. [c]PSEHTT:BFI-P2 at 1:4 (w/w), annealing at 175 °C for 10 min. [d]Fabricated under the best conditions reported in ref 56. [e]PSEHTT:DBFI-T at 1:2 (w/w), annealed at 175 °C for 10 min. [f]PSEHTT:BFI-P2 at 1:4 (w/w), annealed at 150 °C for 10 min.

relatively high-lying LUMO energy level of BFI-P2 and poor contacts between the active layer and the electrode due to the rougher surface of the PSEHTT:BFI-P2 blend film, as revealed by the atomic force microscopy (AFM) imaging to be discussed below. However, in terms of electron transport, molecular size, and density of states at the LUMO, as discussed earlier, BFI-P2 is quite comparable to $PC_{60}BM$. Thus, among the factors missing in the BFI-P2 that could account for its inferior charge photogeneration and photovoltaic properties compared to $PC_{60}BM$ include the nonspherical architecture. By achieving a nonplanar and multichromophoric molecular framework in DBFI-T, we find that this nonfullerene acceptor exhibits far superior charge photogeneration and photovoltaic properties compared to the benchmark $PC_{60}BM$. We speculate that differences in molecular size, planar/nonplanar 3D architecture, HOMO/LUMO energy levels, and density of states at the LUMO of BFI-P2, DBFI-T, and $PC_{60}BM$, as discussed earlier, are among the reasons for the observed difference in photovoltaic performance. These results demonstrate for the first time achievement of a rationally designed, nonfullerene, small-molecule acceptor (DBFI-T) that has superior charge photogeneration and photovoltaic properties than the benchmark fullerene-$PC_{60}BM$.

Bulk Charge Transport and Morphology of Active Layer Blends. The charge transport properties of the donor:acceptor blends were investigated by space-charge-limited current (SCLC) measurements. Hole-only devices with structure of ITO/PEDOT:PSS/blend/Au and electron-only devices with structure of ITO/ZnO/blend/LiF/Al were fabricated and characterized. Figure 5 shows the current–voltage (I–V) characteristics and SCLC fittings of the devices, and the resulting hole and electron mobilities are summarized in Table 2. Both PSEHTT:DBFI-T and PSEHTT:$PC_{60}BM$ blends have sufficiently high and balanced electron and hole mobilities in the range of 1.2×10^{-4} to 2.8×10^{-4} cm²/(V s). In contrast, the PSEHTT:BFI-P2 blend has a much lower electron mobility of 3.5×10^{-7} cm²/(V s), in spite of the high field effect electron mobility in BFI-P2 neat film, than the hole mobility of 1.8×10^{-4} cm²/(V s), which is consistent with the low photovoltaic efficiency in OPVs of the PSEHTT:BFI-P2 cells. The observed orders of magnitude much lower SCLC electron mobility of BFI-P2 in the blend than its neat film in OFETs is consistent with high anisotropy in charge transport of the highly crystalline molecule. These results further demonstrate the critical role of the nonplanar 3D architecture and associated isotropic electron transport in achieving high photovoltaic performance of electron acceptors.

The surface and bulk morphology of the PSEHTT:DBFI-T and PSEHTT:BFI-P2 active layer blends was investigated by AFM, XRD, and transmission electron microscopy (TEM). Sufficient contrast was not observed in the TEM image of the
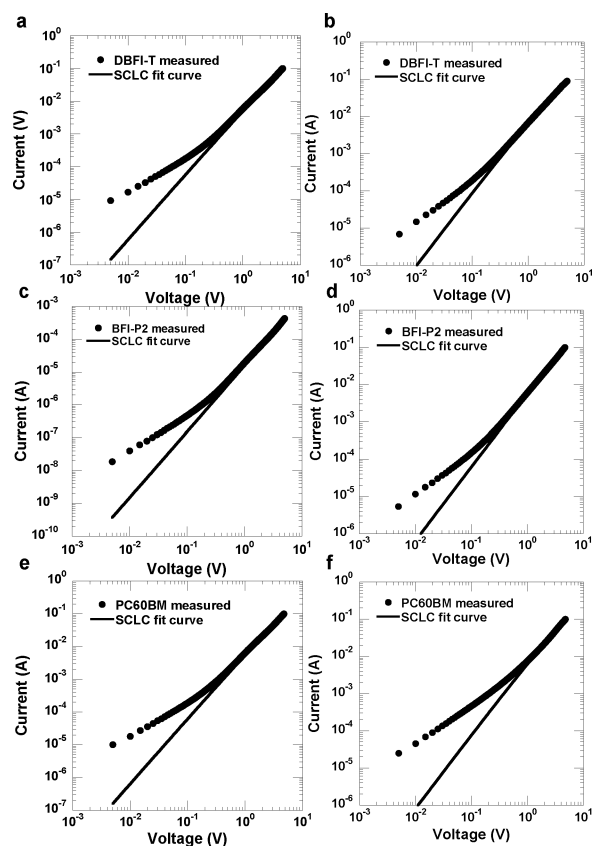

Figure 5. I–V characteristics and SCLC fittings of devices measured in ambient conditions. Electron-only SCLC devices: ITO/ZnO/blend/LiF/Al with PSEHTT:DBFI-T(1:2, w/w) (a), PSEHTT:BFI-P2 (1:4, w/w) (c), and PSEHTT:$PC_{60}BM$ (1:1, w/w) (e) blends. Hole-only SCLC devices: ITO/PEDOT:PSS/blend/Au with PSEHTT:DBFI-T(1:2, w/w) (b), PSEHTT:BFI-P2 (1:4, w/w) (d), and PSEHTT:$PC_{60}BM$ (1:1, w/w) (f) blends.

PSEHTT:DBFI-T active layer. The AFM topographic image revealed good quality PSEHTT:DBFI-T blend film with a smooth surface (Figure 6a), while the corresponding phase image showed a uniform nanoscale phase separation with bicontinuous networks at the surface (Figure 6b). In contrast, the phase image of the PSEHTT:BFI-P2 surface showed coarse phase separation with large domains over 100 nm (Figure 6d). XRD showed that BFI-P2 is highly crystalline in neat films with strong diffraction signals, while DBFI-T films are poorly crystalline with a weak broad signal (Figure S14). Notably, the observed diffractions in the neat films of BFI-P2 and DBFI-T were also seen in the corresponding blends with PSEHTT, suggesting that there is sufficient phase separation in the blends.

14593

dx.doi.org/10.1021/ja508472j | J. Am. Chem. Soc. 2014, 136, 14589–14597

Table 2. Space-Charge-Limited Current Mobilities of Active Layer Blends

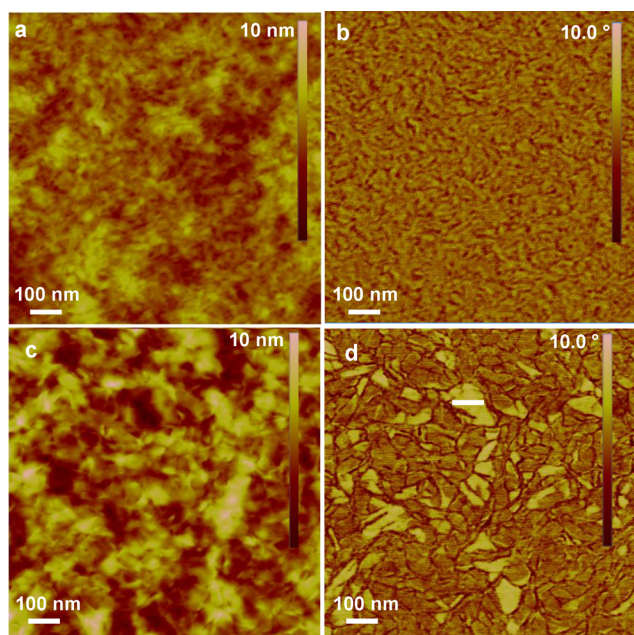| charge carrier	active layer	device layer thickness [nm]	$\mu\ (E = 0)\ [cm^2/(V\ s)]$	$\beta\ [cm^{1/2}/V^{1/2}]$	$E_{max}\ [V/m]$
electron	PSEHTT:DBFI-T	100	1.2×10^{-4}	1.8×10^{-6}	4.9×10^{7}
	PSEHTT:BFI-P2	105	3.5×10^{-7}	8.2×10^{-7}	4.8×10^{7}
	PSEHTT:PC$_{60}$BM	120	2.3×10^{-4}	2.4×10^{-6}	4.1×10^{7}
hole	PSEHTT:DBFI-T	110	2.8×10^{-4}	5.6×10^{-6}	4.9×10^{7}
	PSEHTT:BFI-P2	110	1.8×10^{-4}	2.6×10^{-6}	4.3×10^{7}
	PSEHTT:PC$_{60}$BM	110	2.3×10^{-4}	3.6×10^{-6}	4.3×10^{7}

Figure 6. AFM surface topographic (a and c) and phase (b and d) images of the PSEHTT:DBFI-T (a and b) and PSEHTT:BFI-P2 (c and d) blend films from the best inverted cell.

Figure 7. Xe-flash TRMC measurement of blend films. Photoconductivity transient maxima ($\Delta\sigma_{max}$) of PSEHTT:BFI-P2 and PSEHTT:DBFI-T plotted versus acceptor concentration (a). The lines are a guide for the eye. Photoconductivity transients of 1:2 w/w blends of PSEHTT:BFI-P2, PSEHTT:DBFI-T, and PSEHTT:PC$_{60}$BM (b). (Note that the two peaks are due to the distorted pulse shape of the white light pulse. The temporal profile of the white light pulse is shown in Figure S18). Comparison of $\Delta\sigma_{max}$ (c) with maximum PCEs (d) of actual devices.

The high crystallinity and large phase domains in BFI-P2 blends are due to the relatively planar structure of the acceptor, whereas the nonplanar 3D architecture of DBFI-T lowers the crystallinity and prevents its BHJ blends from forming undesired large phase-separated domains. Although we do not have sufficient information to explain how the surface and bulk morphologies affect the photovoltaic properties of DBFI-T and BFI-P2, such significantly different solid-state morphology between PSEHTT:DBFI-T and PSEHTT:BFI-P2 blends must have played different roles in the process of charge separation, transport, and collection and thus affected the photovoltaic properties.

Time-Resolved Microwave Conductivity (TRMC) Studies. The photoconductive properties of PSEHTT:BFI-P2 and PSEHTT:DBFI-T blends were investigated by means of Xe-flash time-resolved microwave conductivity (TRMC) technique,[59,60] where a 10 μs-width white light pulse (pseudo solar spectrum) from a Xe-flash lamp and 9 GHz microwave were used as an excitation and a probe, respectively. Figure 7a shows the dependences of transient photoconductivity maxima ($\Delta\sigma_{max}$) on the blend ratios of PSEHTT:BFI-P2 and PSEHTT:DBFI-T; related kinetic decays are provided in Figure S15. The $\Delta\sigma_{max}$ of Xe-flash TRMC evaluates the overall optoelectronic performance of the film without fabricating devices, as it includes information about the charge separation yield, local charge carrier mobility, their lifetimes, and sunlight absorption property of the films. PSEHTT:BFI-P2 and
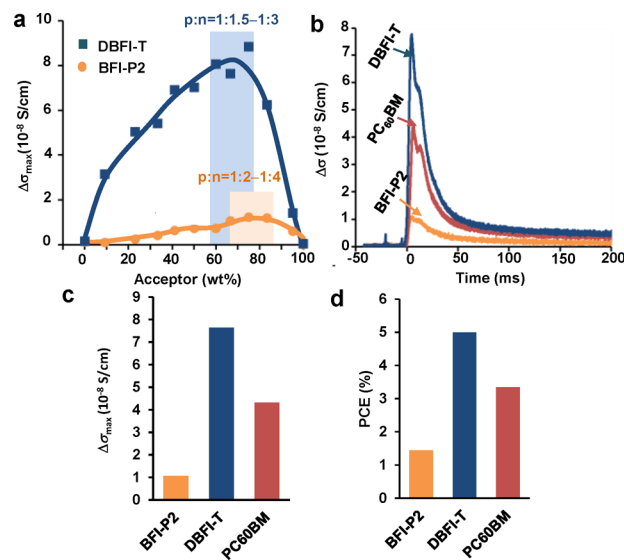
PSEHTT:DBFI-T blends show peaks (best blend ratio) at around donor:acceptor (p:n) = 1:3 and 1:2, respectively. The laser-flash TRMC of these films indicate that the peak position varies with different excitation wavelength (355, 500, and 680 nm), as a result of interplay of charge carrier generation pathway from excitons in p phase (donor) and n phase (acceptor)[59] as shown in Figures S16 and S17. The $\Delta\sigma_{max}$ of laser- and Xe-flash TRMC are, nonetheless, always higher for PSEHTT:DBFI-T than PSEHTT:BFI-P2, indicative of better photovoltaic device performance of DBFI-T. At 500 nm excitation, a 7-fold increase of $\Delta\sigma_{max}$ was observed for PSEHTT:BFI-P2 by blending BFI-P2 with PSEHTT (Figure S16), while PSEHTT:DBFI-T displays as much as 38-fold increase in $\Delta\sigma_{max}$ (Figure S17). These results demonstrate a potential for high photovoltaic efficiency of BHJ blends of PSEHTT and DBFI-T.

The photoconductivity transients of PSEHTT:BFI-P2 and PSEHTT:DBFI-T blends, as compared to the PSEHTT:PC$_{60}$BM (w/w 1:2) reference system at optimal ratio,[56] are shown in Figure 7b. The PSEHTT:DBFI-T blend showed a significantly higher $\Delta\sigma_{max}$ than the PSEHTT:PC$_{60}$BM, whereas PSEHTT:BFI-P2 had the lowest $\Delta\sigma_{max}$ (Figure 7c); the same trend was also observed in the photovoltaic efficiency in BHJ solar cells (Figure 7d), highlighting the excellent charge photogeneration and photovoltaic properties of DBFI-T.

14594

dx.doi.org/10.1021/ja508472j | J. Am. Chem. Soc. 2014, 136, 14589–14597

These results are of particular significance since all prior TRMC evaluation of nonfullerene acceptors has showed them to be inferior to $PC_{60}BM$.[18] Furthermore, we conclude that the observed similar trends in the PCE of BHJ solar cells and transient photoconductivity maximum ($\Delta\sigma_{max}$) of TRMC experiments among the nonfullerene acceptors and $PC_{60}BM$ validate their intrinsic molecular origin and the molecular design strategy.

CONCLUSIONS

In summary, we have rationally designed and experimentally realized a novel, multichromophoric, organic electron-acceptor molecule, DBFI-T, with nonplanar 3D architecture that has showed better performance than $PC_{60}BM$ when paired with PSEHTT in both conventional and inverted OPV cells. The superior charge photogeneration and electron-accepting properties of DBFI-T compared to $PC_{60}BM$ with a common donor polymer (PSEHTT) were confirmed by independent Xe-flash TRMC measurements. The π-conjugated framework of each DBFI-T molecule has a large projected planar surface are a ($\sim 2 \times 2$ nm^2) for interaction with a donor polymer, which is equivalent to that of an aggregate of 9 [C_{60}]-fullerene molecules. The observed high 5.04% PCE along with high photocurrent, FF, EQE, and TRMC imply highly efficient charge photogeneration in DBFI-T/polymer blends. However, the large size (surface area and volume) and poorly crystalline nature of DBFI-T suggest that the detailed mechanism of charge photogeneration in DBFI-T/polymer blends may be very different from that of fullerene-PCBM/polymer systems. The multichromophoric, large size, and nonplanar 3D approach to new electron acceptors demonstrated here could be broadly useful in the design of more efficient OPV materials.

MATERIALS AND METHODS

Materials. Tri(o-Tol)phosphine (P(o-Tol)$_3$), tris-(dibenzylideneacetone) dipalladium (0) (Pd$_2$(dba)$_3$), trimethylphenyltin, and 2,5-bis(trimethylstannyl)thiophene were purchased from Aldrich and used as received. 8,17-Dibromobenzodifluoranthene-3,4,12,13-tetracaboxylic acid diimide (BFI-Br2) was synthesized by following the reported procedures.[54] The synthesis of poly[[(4,4'-bis(2-ethylhexyl)dithieno[3,2-b:2',3'-d]silole)- 2,6-diyl-alt-(2,5-bis(3-(2-ethylhexyl)thiophen-2yl)thiazolo[5,4-d]thiazole)] (PSEHTT) was previously reported.[57]

Synthesis of BFI-P2 and BFI-PBr. Under argon, BFI-Br$_2$ (compound 1, 1.0 g, 0.71 mmol), trimethyl(phenyl)tin (172 mg, 0.71 mmol), Pd$_2$(dba)$_3$ (24 mg), and P(o-tol)$_3$ (32 mg) were transferred into a Schlenk tube and dissolved in 50 mL of degassed toluene. The mixture was heated to 100−120 °C and kept stirring for 24 h. After removing all the volatile materials, the solid residue was purified by thin-film chromatography sequentially with chloroform and chloroform with a few drops of methanol as the eluents.

BFI-P2 was isolated as a red solid. Yield: 380 mg, 38%. ^{1}H NMR (CDCl$_3$, 25 °C, 500 MHz): δ = 8.47 (d, 4H, ^3J = 7.5 Hz), 8.16 (d, 4H, ^3J = 7.5 Hz), 7.82 (br, 4H), 7.70 (m, 6H), 3.87 (d, 4H, ^3J = 7.0 Hz), 1.84 (br, 2H), 1.4−1.0 (m, 80H), 0.86 ppm (m, 12H). ^{13}C NMR (125 MHz, 25 °C, CDCl$_3$): δ 135.8, 141.3, 138.1, 136.2, 136.0, 134.7, 133.4, 132.6, 128.0, 127.4, 125.0, 124.3, 123.2, 44.7, 37.0, 32.2, 32.1, 31.9, 30.3, 29.9, 29.9, 29.9, 29.6, 26.7, 22.9, 14.3 ppm; HRMS (m/z): [M]$^+$ calcd for C$_{94}$H$_{116}$N$_6$O$_4$, 1393.91; found, 1394.55. Elemental analysis calcd for C$_{94}$H$_{116}$N$_6$O$_4$: C 80.99%, H 8.39%, N 6.03%; found C 80.95%, H 8.33%, N 5.93%.

BFI-PBr was isolated as a red solid. Yield: 400 mg, 40%. ^{1}H NMR (CDCl$_3$, 25 °C, 500 MHz): δ = 8.51 (d, 2H, ^3J = 7.5 Hz), 8.41 (d, 2H, ^3J = 7.0 Hz), 8.22 (d, 4H, ^3J = 7.5 Hz), 8.05 (br, 2H), 7.77 (m, 3H), 3.76 (d, ^3J = 6.0 Hz, 4H), 1.79 (br, 2H), 1.4−1.0 (m, 80H), 0.87 ppm (m, 12H). ^{13}C NMR (125 MHz, 25 °C, CDCl$_3$): δ 162.3, 162.2, 153.3,

153.2, 141.4, 137.9 136.8, 135.4, 134.6, 134.1, 133.7, 133.4, 132.5, 132.2, 128.3, 128.0, 127.2, 124.3, 124.2, 124.1, 123.6, 123.2, 44.0, 37.0, 32.2, 32.1, 31.6, 30.4, 30.0, 29.9, 29.6, 29.6, 26.4, 22.9, 14.4 ppm; HRMS (m/z): [M]$^+$ calcd for C$_{88}$H$_{111}$BrN$_6$O$_4$, 1394.79; found, 1397.62.

Synthesis of DBFI-T. Under argon, BFI-PBr (380 mg, 0.27 mmol), 2,5-bis(trimethylstannyl)thiophene (55.0 mg, 0.13 mmol), Pd$_2$(dba)$_3$ (9 mg), and P(o-tol)$_3$ (12 mg) were transferred into a Schlenk tube and dissolved in 16 mL of degassed toluene. The mixture was heated to reflux and kept stirring for 72 h. After removing all the volatile materials, the solid residue was purified by thin-film chromatography with chloroform and a few drops of methanol as the eluent. The product was isolated as a green solid. Yield: 200 mg, 54.9%. ^{1}H NMR (CDCl$_3$, 270 K, 500 MHz): δ = 9.06 (s, 2H, Th), 8.74 (d, 2H, ^3J = 7.5 Hz, BFI), 8.65 (d, 2H, ^3J = 7.5 Hz, BFI), 8.55 (d, 2H, ^3J = 7.0 Hz, BFI), 8.32 (d, 2H, ^3J = 7.5 Hz, BFI), 8.27 (d, 2H, ^3J = 7.0 Hz, BFI), 8.14 (d, 2H, ^3J = 7.0 Hz, BFI), 8.06 (br, 2H, Ph), 8.00 (d, 4H, ^3J = 7.5 Hz, BFI), 7.87 (t, 4H, Ph), 7.79 (d, 4H, ^3J = 7.0 Hz, BFI), 7.67 (br, 2H, Ph), 7.39 (br, 2H, Ph), 4.14 (br, 4H, CH2), 3.31 (br, 2H, CH$_2$), 2.97 (br, 2H, CH$_2$), 2.00 (br, 2H, CH), 1.5−0.75 (m, 186H, CH$_2$+CH$_3$). HRMS (m/z): [M]$^+$ calcd for C$_{180}$H$_{224}$N$_{12}$O$_8$S, 2714.12; found, 2713.61. Analysis (calcd, found for C$_{180}$H$_{224}$N$_{12}$O$_8$S): C (79.60%, 79.71%), H (8.31%, 8.35%), N (6.19%, 6.03%).

Fabrication and Testing of Conventional Solar Cells. BHJ solar cells with the structure of ITO/PEDOT:PSS/active layer/LiF/Al were fabricated. ITO substrates (10 Ω/□, Shanghai B. Tree Tech. Consult Co., Ltd., Shanghai, China) were cleaned sequentially with acetone, deionized water, and isopropyl alcohol in an ultrasonic bath and blown with nitrogen until dried. A 40 nm PEDOT:PSS (Clevios P VP AI 4083) layer was spin-coated on top of the ITO and dried at 150 °C for 10 min under vacuum. The PSEHTT:BFI-P2 active layer was then spin-coated from PSEHTT:BFI-P2 (1:4 w/w) solution in chloroform to make a thin film of ∼120 nm thickness, which was thermally annealed at 150 °C for 10 min in a glovebox. The PSEHTT:DBFI-T active layer was spin-coated from PSEHTT:DBFI-T (1:2, w/w) solution in chloroform to make a thin film of ∼100 nm thickness and then thermally annealed at 175 °C for 10 min in a glovebox. The substrates were then loaded in a thermal evaporator (BOC Edwards, 306) to deposit a cathode composed of 1.0 nm LiF and 90 nm Al under high vacuum (8 × 10^{-7} Torr). Five solar cells, each with an active area of 4 mm^2, were fabricated per ITO substrate. The current density−voltage (J−V) curves of solar cells were measured using a HP4155A semiconductor parameter analyzer under laboratory ambient air conditions. An AM1.5 illumination at 100 mW/cm^2 was provided by a filtered Xe lamp and calibrated by using an NREL-calibrated Si photodiode. The EQE was measured by using a QEX10 solar cell quantum efficiency measurement system (PV Measurements, Inc.) and was calibrated with a NREL-certified Si photodiode before measurement.

Fabrication and Testing of Inverted Solar Cells. BHJ solar cells with the inverted structure of ITO/ZnO/active layer/MoO$_3$/Ag were fabricated. ITO substrates were cleaned similarly as above. Zinc oxide (ZnO) precursor was prepared as we previously reported,[34] spin-coated on top of the ITO, and annealed at 250 °C for 1 h in air. The ZnO film thickness (∼30 nm) was measured with a profilometer. ZnO surface modification was conducted by spin-coating a solution of ethanolamine in 2-methoxyethanol (1 vol %) followed by drying at 110 °C for 10 min. The PSEHTT:BFI-P2 and PSEHTT:DBFI-T active layers were spin-coated from the PSEHTT:BFI-P2 (1:4 w/w) and PSEHTT:DBFI-T (1:2 w/w) blend solutions in chloroform, respectively, and thermally annealed at 175 °C for 10 min in a glovebox. The substrates were then loaded in a thermal evaporator (BOC Edwards, 306) to deposit an anode composed of thin layer (10.0 nm) of MoO$_3$ and 100 nm Ag under high vacuum (8 × 10^{-7} Torr). The devices were tested similarly as the conventional solar cells.

Time-Resolved Microwave Conductivity (TRMC). The blend films of PSEHTT:BFI-P2 and PSEHTT:DBFI-T on quartz plates were prepared by drop-casting of chlorobenzene solutions without solvent additive at desired p:n compositions and dried in a vacuum oven for 2 h at room temperature. A mixing ratio of PSEHTT:PC$_{60}$BM film was

fixed at the reported optimal condition (p:n = 1:2, chlorobenzene, 2.5 v/v% DIO),[56] and films were prepared in the same fashion. A resonant cavity was used to obtain a high degree of sensitivity in the TRMC measurements. The resonant frequency and microwave power were set at ca. 9.1 GHz and 3 mW, respectively, so that the electric field of the microwave was sufficiently small to not disturb the motion of charge carriers. The third harmonic generation (THG; 355 nm) of a Nd:YAG laser (Continuum Inc., Surelite II, 5−8 ns pulse duration, 10 Hz) or 500 and 680 nm pulses from an optical parametric oscillator (Continuum Inc., Panther) seeded by THG of a Nd:YAG laser was used as an excitation source. The laser power was fixed at 2.5 mJ/(cm^{2}pulse) for all excitation wavelengths (incident photon density, $I_0 = $ 4.6, 6.4, and 8.7 × 10^{15} photons/(cm^2 pulse) for 355, 500, and 680 nm, respectively). An in-house-built Xe-flash lamp (10 μs pulse duration, 10 Hz) with a power of 0.3 mJ/(cm^2 pulse) was used for the Xe-flash TRMC experiments. For the attenuation of excitation light energy, neutral density filters were used for both Xe-flash and laser-flash TRMC. The details have been reported in the literature.[60]

■ ASSOCIATED CONTENT

Ⓢ Supporting Information

Characterizations of BFI-PBr and BFI-P2, NMR spectra, TGA traces, DSC scans, optical absorption spectra of BFI-P2 and DBFI-T solutions and cyclic voltammograms of BFI-P2 and DBFI-T thin films, OFET data, J−V curves, and EQE spectra of PSEHTT:BFI-P2 solar cells, DFT, and TD-DFT calculations, simulated Connolly molecular surface and molecular volume of DBFI-T and C$_{60}$. This material is available free of charge via the Internet at http://pubs.acs.org.

■ AUTHOR INFORMATION

Corresponding Author
jenekhe@u.washington.edu

Notes
The authors declare no competing financial interest.

■ ACKNOWLEDGMENTS

■ REFERENCES

(1) Sariciftci, N. S.; Smilowitz, L.; Heeger, A. J.; Wudl, F. *Science* **1992**, *258*, 1474−1476.

(2) Yu, G.; Gao, J.; Hummelen, J. C.; Wudl, F.; Heeger, A. J. *Science* **1995**, *270*, 1789−1791.

(3) Clarke, T. M.; Durrant, J. R. *Chem. Rev.* **2010**, *110*, 6736−6767.

(4) Li, G.; Zhu, R.; Yang, Y. *Nat. Photonics* **2012**, *6*, 153−161.

(5) Günes, S.; Neugebauer, H.; Sariciftci, N. S. *Chem. Rev.* **2007**, *107*, 1324−1338.

(6) Peet, J.; Kim, J. Y.; Coates, N. E.; Ma, W. L.; Moses, D.; Heeger, A. J.; Bazan, G. C. *Nat. Mater.* **2007**, *6*, 497−500.

(7) Shaheen, S. E.; Brabec, C. J.; Sariciftci, N. S.; Padinger, F.; Fromherz, T.; Hummelen, J. C. *Appl. Phys. Lett.* **2001**, *78*, 841−843.

(8) Ma, W.; Yang, C.; Gong, X.; Lee, K.; Heeger, A. J. *Adv. Funct. Mater.* **2005**, *15*, 1617−1622.

(9) Liang, Y.; Xu, Z.; Xia, J.; Tsai, S.-T.; Wu, Y.; Li, G.; Ray, C.; Yu, L. *Adv. Mater.* **2010**, *22*, E135−E138.

(10) He, Z.; Zhong, C.; Su, S.; Xu, M.; Wu, H.; Cao, Y. *Nat. Photonics* **2012**, *6*, 591−595.

(11) Guo, X.; Zhou, N.; Lou, S. J.; Smith, J.; Tice, D. B.; Hennek, J. W.; Ortiz, R. P.; Navarrete, J. T. L.; Li, S.; Strzalka, J.; Chen, L. X.; Chang, R. P. H.; Facchetti, A.; Marks, T. J. *Nat. Photonics* **2013**, *7*, 825−833.

(12) Sonar, P.; Fong Lim, J. P.; Chan, K. L. *Energy Environ. Sci.* **2011**, *4*, 1558−1574.

(13) Ahmed, E.; Ren, G.; Kim, F. S.; Hollenbeck, E. C.; Jenekhe, S. A. *Chem. Mater.* **2011**, *23*, 4563−4577.

(14) Anthony, J. E. *Chem. Mater.* **2011**, *23*, 583−590.

(15) Zheng, Y.-Q.; Dai, Y.-Z.; Zhou, Y.; Wang, J.-Y.; Pei, J. *Chem. Commun.* **2014**, *50*, 1591−1594.

(16) Zhang, X.; Lu, Z.; Ye, L.; Zhan, C.; Hou, J.; Zhang, S.; Jiang, B.; Zhao, Y.; Huang, J.; Zhang, S.; Liu, Y.; Shi, Q.; Liu, Y.; Yao, J. *Adv. Mater.* **2013**, *25*, 5791−5797.

(17) Bloking, J. T.; Han, X.; Higgs, A. T.; Kastrop, J. P.; Pandey, L.; Norton, J. E.; Risko, C.; Chen, C. E.; Brédas, J.-L.; McGehee, M. D.; Sellinger, A. *Chem. Mater.* **2011**, *23*, 5484−5490.

(18) Suzuki, T.; Okamoto, T.; Saeki, A.; Seki, S.; Sato, H.; Matsuo, Y. *ACS Appl. Mater. Interfaces* **2013**, *5*, 1937−1942.

(19) Schwenn, P. E.; Gui, K.; Nardes, A. M.; Krueger, K. B.; Lee, K. H.; Mutkins, K.; Rubinstein-Dunlop, H.; Shaw, P. E.; Kopidakis, N.; Burn, P. L.; Meredith, P. *Adv. Energy Mater.* **2011**, *1*, 73−81.

(20) Zhou, Y.; Ding, L.; Shi, K.; Dai, Y.-Z.; Ai, N.; Wang, J.; Pei, J. *Adv. Mater.* **2012**, *24*, 957−961.

(21) Ren, G.; Ahmed, E.; Jenekhe, S. A. *Adv. Energy Mater.* **2011**, *1*, 946−953.

(22) Woo, C. H.; Holcombe, T. W.; Unruh, D. A.; Sellinger, A.; Fréchet, J. M. J. *Chem. Mater.* **2010**, *22*, 1673−1679.

(23) Lin, Y.; Cheng, P.; Li, Y.; Zhan, X. *Chem. Commun.* **2012**, *48*, 4773−4775.

(24) Eftaiha, A. a. F.; Sun, J.-P.; Hill, I. G.; Welch, G. C. *J. Mater. Chem. A* **2014**, *2*, 1201−1213.

(25) Pho, T. V.; Toma, F. M.; Tremolet de Villers, B. J.; Wang, S.; Treat, N. D.; Eisenmenger, N. D.; Su, G. M.; Coffin, R. C.; Douglas, J. D.; Fréchet, J. M. J.; Bazan, G. C.; Wudl, F.; Chabinyc, M. L. *Adv. Energy Mater.* **2014**, *4*, 1301007.

(26) Bloking, J. T.; Giovenzana, T.; Higgs, A. T.; Ponec, A. J.; Hoke, E. T.; Vandewal, K.; Ko, S.; Bao, Z.; Sellinger, A.; McGehee, M. D. *Adv. Energy Mater.* **2014**, *4*, 1301426.

(27) Mao, Z.; Senevirathna, W.; Liao, J.-Y.; Gu, J.; Kesava, S. V.; Guo, C.; Gomez, E. D.; Sauvé, G. *Adv. Mater.* **2014**, DOI: 10.1002/adma.201400647.

(28) Sullivan, P.; Duraud, A.; Hancox, l.; Beaumont, N.; Mirri, G.; Tucker, J. H. R.; Hatton, R. A.; Shipman, M.; Jones, T. S. *Adv. Energy Mater.* **2011**, *1*, 352−355.

(29) Verreet, B.; Rand, B. P.; Cheyns, D.; Hadipour, A.; Aernouts, T.; Heremans, P.; Medina, A.; Claessens, C. G.; Torres, T. *Adv. Energy Mater.* **2011**, *1*, 565−568.

(30) Verreet, B.; Cnops, K.; Cheyns, D.; Heremans, P.; Stesmans, A.; Zango, G.; Claessens, C. G.; Torres, T.; Rand, B. P. *Adv. Energy Mater.* **2014**, *4*, 1301413.

(31) Facchetti, A. *Mater. Today* **2013**, *16*, 123−132.

(32) Zhou, E.; Cong, J.; Wei, Q.; Tajima, K.; Yang, C.; Hashimoto, K. *Angew. Chem., Int. Ed.* **2011**, *50*, 2799−2803.

(33) Zhou, N.; Lin, H.; Lou, S. J.; Yu, X.; Guo, P.; Manley, E. F.; Loser, S.; Hartnett, P.; Huang, H.; Wasielewski, M. R.; Chen, L. X.; Chang, R. P. H.; Facchetti, A.; Marks, T. J. *Adv. Energy Mater.* **2014**, *4*, 1300785.

(34) Earmme, T.; Hwang, Y.-J.; Murari, N. M.; Subramaniyan, S.; Jenekhe, S. A. *J. Am. Chem. Soc.* **2013**, *135*, 14960−14963.

(35) Zhou, Y.; Kurosawa, T.; Ma, W.; Guo, Y.; Fang, L.; Vandewal, K.; Diao, Y.; Wang, C.; Yan, Q.; Reinspach, J.; Mei, J.; Appleton, A. L.; Koleilat, G. I.; Gao, Y.; Mannsfeld, S. C. B.; Salleo, A.; Ade, H.; Zhao, D.; Bao, Z. *Adv. Mater.* **2014**, *26*, 3767−3772.

(36) Mori, D.; Benten, H.; Okada, I.; Ohkita, H.; Ito, S. *Adv. Energy Mater.* **2014**, *4*, 1301006.

(37) Hwang, Y.-J.; Earmme, T.; Subramaniyan, S.; Jenekhe, S. A. *Chem. Commun.* **2014**, *50*, 10801−10804.

(38) Earmme, T.; Hwang, Y.-J.; Subramaniyan, S.; Jenekhe, S. A. *Adv. Mater.* **2014**, *26*, 6080−6085.

(39) Zang, Y.; Li, C.-Z.; Chueh, C.-C.; Williams, S. T.; Jiang, W.; Wang, Z.-H.; Yu, J.-S.; Jen, A. K. Y. *Adv. Mater.* **2014**, *26*, 5708−5714.

(40) Brabec, C. J.; Gowrisanker, S.; Halls, J. J. M.; Laird, D.; Jia, S.; Williams, S. P. *Adv. Mater.* **2010**, *22*, 3839−3856.

(41) Scharber, M. C.; Mühlbacher, D.; Koppe, M.; Denk, P.; Waldauf, C.; Heeger, A. J.; Brabec, C. J. *Adv. Mater.* **2006**, *18*, 789−794.

(42) Liang, Y.; Yu, L. *Acc. Chem. Res.* **2010**, *43*, 1227−1236.

(43) Liu, T.; Troisi, A. *Adv. Mater.* **2013**, *25*, 1038−1041.

(44) Kanai, Y.; Grossman, J. C. *Nano Lett.* **2007**, *7*, 1967−1972.

(45) Holcombe, T. W.; Norton, J. E.; Rivnay, J.; Woo, C. H.; Goris, L.; Piliego, C.; Griffini, G.; Sellinger, A.; Brédas, J.-L.; Salleo, A.; Fréchet, J. M. J. *J. Am. Chem. Soc.* **2011**, *133*, 12106−12114.

(46) Bakulin, A. A.; Rao, A.; Pavelyev, V. G.; van Loosdrecht, P. H. M.; Pshenichnikov, M. S.; Niedzialek, D.; Cornil, J.; Beljonne, D.; Friend, R. H. *Science* **2012**, *335*, 1340−1344.

(47) Pensack, R. D.; Guo, C.; Vakhshouri, K.; Gomez, E. D.; Asbury, J. B. *J. Phys. Chem. C* **2012**, *116*, 4824−4831.

(48) Cowan, S. R.; Banerji, N.; Leong, W. L.; Heeger, A. J. *Adv. Funct. Mater.* **2012**, *22*, 1116−1128.

(49) Gregg, B. A. *J. Phys. Chem. Lett.* **2011**, *2*, 3013−3015.

(50) Roncali, J.; Leriche, P.; Cravino, A. *Adv. Mater.* **2007**, *19*, 2045−2060.

(51) Kanibolotsky, A. L.; Perepichka, I. F.; Skabara, P. J. *Chem. Soc. Rev.* **2010**, *39*, 2695−2728.

(52) Savoie, B. M.; Rao, A.; Bakulin, A. A.; Gelinas, S.; Movaghar, B.; Friend, R. H.; Marks, T. J.; Ratner, M. A. *J. Am. Chem. Soc.* **2014**, *136*, 2876−2884.

(53) Jenekhe, S. A.; Osaheni, J. A. *Science* **1994**, *265*, 765−768.

(54) Li, H.; Kim, F. S.; Ren, G.; Hollenbeck, E. C.; Subramaniyan, S.; Jenekhe, S. A. *Angew. Chem., Int. Ed.* **2013**, *52*, 5513−5517.

(55) Goel, A.; Howard, J. B.; Vander Sande, J. B. *Carbon* **2004**, *42*, 1907−1915.

(56) Xin, H.; Subramaniyan, S.; Kwon, T.-W.; Shoaee, S.; Durrant, J. R.; Jenekhe, S. A. *Chem. Mater.* **2012**, *24*, 1995−2001.

(57) Subramaniyan, S.; Xin, H.; Kim, F. S.; Shoaee, S.; Durrant, J. R.; Jenekhe, S. A. *Adv. Energy Mater.* **2011**, *1*, 854−860.

(58) von Hauff, E.; Dyakonov, V.; Parisi, J. *Sol. Energy Mater. Sol. Cells* **2005**, *87*, 149−156.

(59) Saeki, A.; Tsuji, M.; Seki, S. *Adv. Energy Mater.* **2011**, *1*, 661−669.

(60) Saeki, A.; Yoshikawa, S.; Tsuji, M.; Koizumi, Y.; Ide, M.; Vijayakumar, C.; Seki, S. *J. Am. Chem. Soc.* **2012**, *134*, 19035−19042.